P1.13 Validation of the Community Radiative Transfer Model (CRTM) against AVHRR Clear-Sky Processor for Oceans (ACSPO) Nighttime Radiances for improved cloud detection and physical SST retrievals

XingMing Liang[1,2*], Alexander Ignatov[1], Yury Kihai[1,3], Andrew Heidinger[1], Yong Han[1] , Yong Chen[1,2]

[1] *NOAA/NESDIS, Center for Satellite Application and Research (STAR), Camp Springs, MD 20746*
[2] *CSU, Cooperative Institute for Research in the Atmospheres (CIRA), Fort Collins, CO 80523*
[3] *Perot Systems Inc (QSS Group), Camp Springs, MD 20746*

1. Introduction

Currently in development at NESDIS, the new AVHRR Clear-Sky Processor for Oceans (ACSPO) will replace the heritage Main Unit Task (MUT) system used at NESDIS since the early 1980s and at NAVO since mid-1990s under the name of SEATEMP (McClain et al., 1985; Walton et al., 1998; May et al., 1998; Ignatov et al., 2004). Similar to the MUT, ACSPO generates AVHRR clear-sky radiances over oceans, from which sea surface temperatures (SST) and aerosol products are derived. A major improvement in ACSPO over the MUT is the full integration of global clear sky AVHRR radiances with the National Centers for Environmental Prediction Global Forecast System (NCEP/GFS) fields. A fast Community Radiative Transfer Model (CRTM), developed at the NESDIS Joint Center for Satellite Data Assimilation (JCSDA) and similar in its overall philosophy to the RTTOV (radiative transfer model for TOVS; Saunders et al., 1999, 2007), is then run with NCEP/GFS inputs to predict TOA clear-sky brightness temperatures (BT) in AVHRR bands 3B (3.7 μm), 4 (11 μm) and 5 (12 μm). Currently, the CRTM BTs are used for quality control (QC) of AVHRR BTs and for improvements to ACSPO cloud mask. Physical SST retrievals are also being explored, in addition to the regression Multi-Channel (MCSST) and Nonlinear SST (NLSST) retrievals, which have been preserved in ACSPO from the MUT. Accuracy of CRTM and GFS input for all these applications is crucial. Careful implementation and validation of the forward CRTM is thus the focus of this study.

The paper is organized as follows. Section 2 introduces the radiative transfer equation for band-averaged radiances used in CRTM. It also describes the NCEP GFS data and how they are collocated with AVHRR observations within ACSPO.

*Corresponding author address: XingMing Liang, NOAA/NESDIS/STAR, WWB Rm. 603, 5200 Auth Rd, Camp Springs, MD 20746; e-mail: Xingming.liang@noaa.gov.

Section 3 describes the implementation of CRTM/GFS in ACSPO and its optimization through a number of sensitivity analyses towards minimization of the M-O bias. In particular, accurate treatment of finite NCEP GFS layers in CRTM and using Fresnel's model instead of black surface reflectance model improve the M-O statistics in all AVHRR bands and for all platforms. Using Reynolds-Smith (version 2) weekly SST (referred herein as the "Reynolds SST") rather than NCEP GFS SST (referred below as the "NCEP SST"), also improves the M-O bias. The improvement is most noticeable in the coastal areas. In section 4, the M-O bias is analyzed in a variety of environmental and geographical conditions and in the full AVHRR swath. We conclude that, overall, the CRTM performs accurately and relatively uniformly in the full range of retrieval conditions representative of their global variability and across the swath. Section 5 checks the stability of the M-O bias over a period of one week, and section 6 summarizes the results of this study.

2. Forward Model and Input Data

Neglecting extraterrestrial radiation at night, omitting effects of scattering in the atmosphere, and assuming that the oceanic surface is flat (i.e., its emissivity obeys Fresnel's model), the radiative transfer equation (RTE) for a wide-band sensor such as AVHRR is written as follows

$$\overline{R}(\theta)=\overline{\varepsilon}(\theta)\overline{B}(T_s)\overline{\tau}(\theta)+\overline{L}^{\uparrow}(\theta)+(1-\overline{\varepsilon}(\theta))\overline{L}^{\downarrow}(\theta)\overline{\tau}(\theta) \quad (1)$$

Here, $\overline{R}(\theta)$ is TOA radiance at sensor level; θ is sensor view zenith angle; $\overline{B}(T_s)$ is Planck radiance; T_s is SST; $\overline{\tau}(\theta)$, $\overline{L}^{\uparrow}(\theta)$ and $\overline{L}^{\downarrow}(\theta)$ are atmospheric transmittance, upwelling, and downwelling radiance, respectively; and $\overline{\varepsilon}(\theta)$ is surface emissivity. Each term in Equation (1) with the overbar sign represents a band average value (i.e., convolved with the respective sensor spectral response $\Phi(\theta)$. The assumption that the monochromatic form of the RTE holds for wide-band radiances is made in any fast RTM

such as the RTTOV or CRTM, because line-by-line (LBL) calculations are computationally unaffordable for real-time applications. For CRTM, channel average transmittances in the thermal IR are calculated using a fast and accurate Optimal Spectral Sampling (OSS) algorithm developed by Atmosphere and Environment Research Inc. (Moncet et al., 2004). CRTM comparisons against LBLRTM have shown that CRTM BTs have an RMS error of ~0.03K with respect to LBLRTM (note that the bias by definition is zero as CRTM is trained against the LBLRTM). (www.orbit.nesdis.noaa.gov/smcd/spb/CRTM/).

2.1 Band average surface emissivity model

Following the CRTM philosophy, band average emissivity is written as follows,

$$\bar{\varepsilon}(\theta) = \frac{\int_{\Delta\nu} \varepsilon(\nu,\theta)\Phi(\nu)d\nu}{\int_{\Delta\nu} \Phi(\nu)d\nu} \qquad (2)$$

Here, ν is the wavenumber and $\Delta\nu$ is the wavenumber range for a band. For Fresnel's surface, spectral emissivity, $\varepsilon(\nu,\theta)$, is calculated from horizontally and vertically polarized reflection coefficients using Fresnel's equation (c.f., Masuda et al., 1988). Note that Fresnel's model does not account for wind speed dependence, which may result in emissivity error and subsequently affect the M-O bias (Masuda et al., 1988). However, further analyses by e.g. Watts et al. (1996) and Wu and Smith (1997) have shown that the wind effect on emissivity is small (error in BT: 0.1K+0.1Kσ) in a sensor zenith angle range from -55º to 55º, even when wind speed is large. The ACSPO processes AVHRR data in a full swath, up to ±68º. In section 4, the wind speed dependence of the bias will be analyzed in the full swath, including large zenith angles.

Using the band average emissivity model may introduce some additional errors in CRTM BT. However, this approach has been extensively used in wide-band RTMs and the associated errors in the TOA BTs are deemed to be small (Sherlock, 1999; Wan and Dozier, 1996).

2.2 NCEP/GFS data

The associated surface variables (surface pressure, temperature, u- and v-wind speeds), and atmospheric profiles of pressure, air temperature, geopotential height, water vapor, and O_3 are specified from the NCEP/GFS files (www.emc.ncep.noaa.gov/modelinfo/). GFS data are available at 1º latitude-longitude spatial resolution at 26 levels of atmospheric pressure and temperature from 1000 to 10 mb, at 20 levels of relative humility from 1000 to 100 mb, and at 6 levels of O_3 from 100 to 10 mb. GFS data are generated four times a day for different forecast times. GFS fields are linearly interpolated in time to match AVHRR observation time, using two 12-hour forecasts separated by 6 hours. The fields interpolated in time are then used as CRTM input to generate TOA BTs at 1º resolutions. The simulated 1º BTs are then interpolated in space to match the AVHRR 4 km GAC pixel.

Atmospheric profiles of pressure, air temperature, RH, and O_3 amount are reported in GFS for atmospheric levels corresponding to boundaries of the atmospheric layers. The level-specific variables need to be converted to effective layer-specific variables before they are used as input to CRTM. Some of these level-to-layer conversions are performed within the CRTM and yet some are left to the CRTM user. Section 3.1 explores sensitivity to a particular implementation.

In addition to H_2O and O_3, CRTM also accounts for the absorption due to five minor and uniformly mixed gases (CO_2, O_2, CO, CH_4, and N_2O). This is done by interpolation between 48 representative atmospheric profiles.

2.3 AVHRR data

In this study, the CRTM is validated against the ACSPO clear-sky BTs in Ch3B, Ch4, and Ch5 onboard NOAA-16,-17, -18 and MetOp-A. These are derived from AVHRR L1B GAC (Global Area Coverage) 4km data. The equator crossing time (EXT) for NOAA-16 -17, -18 and MetOp-A in the nighttime are ~4am, ~10pm, ~2am and ~9:30pm, respectively. We used one week of ACSPO BTs data from 16–22 February 2007 (corresponding Julian days are from JD=47 to JD=53).

The BTs are calibrated, navigated, and quality-controlled using information available from L1B files. The sensor view zenith angle, solar zenith angle, UTC time, and latitude and longitude of the pixels are also saved in ACSPO from L1B data. The ACSPO cloud-mask is currently being documented and will be reported elsewhere.

To eliminate solar contamination, nighttime data are specified as those pixels with solar zenith angle >118º (Cao et al., 2001; Dash and Ignatov, 2008). As a result, about 2 million GAC clear-sky nighttime pixels are available globally within a 24 hour period (~14 orbits) from each platform.

3. CRTM Implementation in ACSPO

The input data to CRTM include atmospheric profiles, SST, and modeled surface emissivity. The way

in which these variables are specified in CRTM may affect the M-O bias. This section discusses the CRTM implementation in order to minimize the M-O bias.

3.1 Treatment of water vapor

NCEP/GFS reports atmospheric pressure and temperature at 26 levels and RH at 20 levels. The level of GFS RH needs to be converted to layer the mass mixing ratio of water vapor before being input to CRTM. The mass mixing ratio of water vapor is proportional to RH and the saturation mixing ratio of water vapor, and can be represented as follows:

$$\gamma = RH \frac{MW_{h2o}}{MW_{dry}} \frac{e_s(T)}{P - e_s(T)} \qquad (3)$$

Here, MW_{h2o} and MW_{dry} are molecular weight of water and effective molecular weight of dry air, respectively, P is atmospheric pressure, and $e_s(T)$ is saturation vapor pressure (SVP) over water, which is a function of air temperature, T.

In the earlier SVP calculations, Goff-Gratch empirical formulation (1946) was customarily used. The newer measurements by Guildner et al. (1976) were fit polynomially (Flatau et al., 1992). Table 1 compares the two SVP values for several air temperatures. The largest difference up to 14% takes place at low temperatures. Since those are typically associated with low water vapor content, the effect on the TOA BTs is only 0.02K.

The dependence of the SVP on temperature shown in Table 1 is exponential. In the initial ACSPO implementation, layer temperatures were first calculated as an average of the two levels and used to calculate the SVP and subsequently the mass mixing ratio for a layer using Equation (3). As an example, Figure 1 (left) shows the M-O biases in Ch5 for one day and three platforms (NOAA-16 through 18) using this initial implementation. The bias strongly depends upon water vapor with amplitude of up to 3K.

A more appropriate approach is to first calculate the SVP and mass mixing ratio at each level, and then calculate the layer effective water vapor content, assuming its exponential decay with the height. Figure 1 (right) shows that using this latter approach reduces the M-O bias by a factor of 2 (from ~3K down to 1.5K).

We thus conclude that a consistent treatment of finite layers in NCEP/GFS profiles improves CRTM-AVHRR comparison. It is also expected that for higher vertical resolution atmospheric profiles, such as ECMWF data, this level-to-layer conversion will be less sensitive to uncertainty. Hereinafter, all analysis presented are based on the second approach, which appears to be more accurate.

3.2 Black vs. Fresnel's surface model

Figure 1 shows that the consistent treatment of NCEP/GFS finite layer in CRTM affects the M-O bias progressively more towards higher water vapor. The low-water-vapor end remains unchanged and biased high by ~1.5K. One of the possible causes is the black surface assumption. Figures 2 and 3 compare M-O bias for black and Fresnel's surfaces in three AVHRR bands and four platforms. We conclude that using Fresnel's instead of black surface model reduces the water vapor and sensor zenith angle structures of the M-O biases.

3.3 Using Reynolds instead of NCEP SST

First-guess SST field integrated in ACSPO comes from the GFS parameter called "surface temperature," which comes from land surface temperature over land and from Reynolds-Smith SST over ocean. Once these 1° resolution data are interpolated to match 4 km GAC pixel data and are used as input to CRTM, large errors in SST may occur in the coastal areas where land values may be used in the interpolation. Whether a gridded value came from a land pixel or from a sea pixel could be, in principle, determined by the land-sea mask. However, in this study we have chosen to implement an optional additional input of Reynolds-Smith weekly V.2 SST to ACSPO (found at ftp://ftp.emc.ncep.noaa.gov/cmb/sst/oisst_v2/.)

Figure 4 shows global histograms of M-O biases for NCEP SST and Reynolds SST input to CRTM. Using Reynolds-SST results in an increased bias and thus leaves a wider margin for the future aerosol inclusion in the model. Also, there is a large improvement in the M-O standard deviation in comparison to NCEP SST, which is equivalent to removing half of error, in an RMS sense.

Figure 5 shows column water vapor and sensor zenith angle dependences of the M-O bias. The M-O biases for Reynolds SST input are larger than that from NCEP SST in the case of low column water vapor. Figure 6 shows that M-O is biased low at low wind speed. To explain this further, global maps of M-O biases for Ch3B in NOAA-18 with Reynolds and NCEP SST inputs to CRTM are shown in Figure 7, and water vapor and wind speed distributions in Figures 8 and 9. One of the differences between the two panels of Figure 7 is near the coasts, where the M-O biases are unrealistically low in case of NCEP SST. Moreover, in these areas, the column water vapor contents and wind

speed are also low as shown in Figures 8 and 9. These areas are associated with lower M-O biases and larger standard deviation for NCEP SST compared to Reynolds SST. Note that without including aerosols in CRTM, Ch3B is expected to have some positive M-O bias, and a smaller M-O does not necessarily mean a better agreement. We thus conclude that interpolation in the coastal area for NCEP SST needs to be improved, or Reynolds SST should be used instead as input to CRTM.

The next section uses the most effective CRTM/GFS implementation, based on consistent treatment of finite layers in NCEP/GFS atmospheric profiles, using Fresnel's emissivity model (instead of black surface assumption), and using Reynolds SST instead of NCEP SST as input to CRTM.

4. Bias in Different Retrieval Conditions

The objective of this section is to evaluate the M-O bias globally and analyze it as a function of those individual observational parameters that are critically important for the accuracy of SST retrievals. Validation described in this section was performed in the full global retrieval domain, and no data were withheld from these analyses. Large errors are thus possible in some retrieval conditions. The objective here was not to perform a bias correction, but rather comprehensively document the global variability of the M-O bias.

4.1 Global histograms of the M-O bias

Figure 4 (right) shows the global mean biases are on the order of 0.2K, 0.35K and 0.35K in Ch3B, Ch4, and Ch5 and their respective standard deviations are less than 0.6K, 0.7K and 0.8K. Cross-platform consistency is best in Ch5, followed by Ch4 and Ch3B. This indicates that the sensor calibrations and spectral response functions are consistent between different platforms. The only exception is the anomaly in NOAA 16-Ch3B, which is also present in all following bias analyses in this section. In a similar study using MODTRAN-AVHRR validation (Dash and Ignatov, 2008), the same NOAA16-Ch3B anomaly was observed and attributed to a possible shift of its spectral response function. Below, this anomalous result is shown but not discussed.

4.2 Environmental structure of the bias

The water vapor dependence of the M-O bias is shown in the left panel of Figure 4 and the corresponding global histogram of 'W' is shown in Figure 10. The M-O bias shows very close agreement between all four platforms, but it behaves differently in different bands. In Ch3B, it is rather flat and largely independent of water vapor, with amplitude not exceeding ~0.5K. However, in Ch4 and Ch5, the amplitude is ~0.8K, likely because these channels are more sensitive to water vapor. The larger biases in low water vapor conditions may be due to errors in SST, missing aerosols, and other absorbing gases. Their effects are expected to be larger in more transparent atmospheres.

Figure 11 shows SST dependence of M-O bias, and the corresponding histogram of SST distribution. Unlike the water vapor histogram in Figure 10, which shows gradual change from the center towards the wings in the full range of column water vapor content, SST is much more densely populated in the high SST range from 290–305K; the sample with SST<290K accounts for only ~15% of the total population. Despite a much smaller sample size at lower SSTs, the bias still shows remarkable cross-platform consistency. The amplitudes of the biases are about 0.5K in Ch3B and 0.9K in Ch4 and Ch5, in the full SST range. The different behavior in the 270–280K range from that in the 280–310K range may be due to the fact that the AVHRR BTs are mainly influenced by SST in low SSTs and progressively more affected the near-surface air temperature and humidity in high SSTs.

Figure 12 shows the sea-air temperature difference (SST-AT) dependence of the M-O bias and its corresponding histogram. The SST-AT is mostly populated in the range of -2 to +4 K. In all three channels and in the entire SST-AT domain, the amplitude of the bias does not exceed 1K. The anomalous atmospheric conditions with large SST-AT differences are mainly associated with the coastal locations (May and Holyer, 1993) and differences in atmospheric and oceanic dynamics (e.g. Philip et al., 2004). Again, good cross-platform consistency takes place in the whole SST-AT domain.

Figure 6 (right panel) shows the wind speed dependence of M-O bias. The corresponding wind speed histogram is shown in Figure 10. Good cross-platform consistency takes place in all three channels. The amplitude of the wind speed dependence does not exceed about 0.6K, including the large wind speed corresponding to a very rough sea surface. The newer studies suggest that the wind speed effect on the sea surface emissivity is smaller than initially thought and can be omitted when sensor view angle is less than 55º (Watts et al., 1996). Our results do not show any significant wind speed dependence, even in the full AVHRR view angles ranging from -68º to +68º. Recall that the current input to CRTM is bulk SST. Using skin SST may modify the

wind speed dependence of M-O bias, as the difference between the two SSTs is least predictable at low winds when large gradients at the surface may exist (Donlon et al., 2002, Emery et al., 2001).

4.3 View zenith angle structure of the bias

In ACSPO, the full AVHRR swath from -68º to +68º is used. Sensor zenith angle effect the TOA radiance through the increased atmospheric path-length and decreased surface emissivity. It is critically important that CRTM performs uniformly in the full range of AVHRR view geometrics.

The right panel of Figure 5 shows the sensor zenith angle dependence and its corresponding histogram is shown in Figure 10. The curves are near-symmetrical with respect to nadir, and the amplitude of the biases is within 0.3K in Ch3B and 0.5K in Ch4 and Ch5.

4.4 Zonal structure of the bias

Global distributions of the environmental parameters (water vapor contents, SST, air temperature, pressure, and wind speed) define global distribution of the M-O bias. Figure 13 shows the global map of M-O bias for three bands in NOAA-16 on 18 February 2007, and Figure 14 shows zonal dependence of the bias and the corresponding histogram. The bias is smallest near the equator and increases towards higher latitude. The cross-platform consistency remains good in all three bands and in the full latitude range.

5. Time Series of the M-O Bias

The above analyses have demonstrated high accuracy and precision of the CRTM forward model and good cross-platform consistency. Animations of each type of histogram and dependence plots of the M-O biases for individual days from this week's data have been made to evaluate the stability of this result. These animations are available on the NESDIS web site at *www.orbit.nesdis.noaa.gov/sod/sst/xliang/*. The noise in the daily data is larger because the number of clear-sky pixels is proportionately reduced compared to that of weekly data. However, the cross-platform consistency remains good in daily data.

Figure 15 shows a time series of the mean bias and its standard deviation for all seven days. The curves of the mean biases in Ch3B are flatter than in Ch4 and Ch5. A more stable CRTM performance in Ch3B is likely due to the smaller water vapor absorption in this band compared to the other two bands. The bias in Ch3B is < 0.3K, and in Ch4 and Ch5 it is < 0.5K. The respective standard deviations are about 0.6, 0.7 and 0.8K, respectively. These biases are very similar to those of weekly data analyses shown in Figure 4. The forward model thus appears precise, stable, and suitable for long-term monitoring of AVHRR BT and for physical SST retrievals.

6. Discussion and Conclusions

CRTM is integrated into ACSPO in conjunction with NCEP GFS fields. It is accurate, precise, and computationally efficient and suitable for global real-time processing of large data volumes. The objectives of this paper were to check and improve the implementation of the CRTM with NCEP/GFS fields and to validate the accuracy of the forward model against AVHRR BTs. The M-O bias was evaluated as a function of main factors responsible for the M-O bias using one week of data from 16–22 February 2007.

With careful treatment of the NCEP/GFS fields and Reynolds SST in the CRTM, an accurate implementation is obtained and the M-O biases are minimized. CRTM is a highly accurate model which closely reproduces AVHRR BTs in Ch3B, Ch4, and Ch5 for NOAA16-18 and MetOp-A. The M-O bias also shows good cross-platform consistency, in all cases. The M-O biases are only slightly dependent on the environmental parameters (column water vapor contents, SST, SST-AT, wind speed), sensor zenith angle, and latitude in all three bands of the four platforms. The global mean M-O biases are on the order of 0.2, 0.35, and 0.35K in Ch3B, Ch4, and Ch5, respectively. An exception is the NOAA16-Ch3B, which shows an anomalous behavior. Analyses of data from individual days show that the CRTM is stable and cross-platform consistencies of the M-O bias remain for all seven days.

The M-O biases tend to be positive in all bands. These warm biases will be reduced when the aerosol model is included in CRTM and the skin SST is used in the modeling. Minimizing cloud contamination and controlling the quality of input GFS will further reduce the M-O biases. We also consider testing this model with other high-resolution numerical weather prediction (NWP) models, such as European Center for Medium-Range Weather Forecasting (ECMWF) data.

From the current analysis, we believe that the CRTM/GFS implementation in ACSPO is good enough to start exploring physical SST retrievals. However, we expect that adding aerosol and reflected solar radiation in the CRTM will be required for accurate physical SST retrievals.

Acknowledgements. This work is done under the Algorithm Working Group funded by the GOES-R

Program Office. X. M. Liang acknowledges the CIRA visiting scientist fellowship. CRTM is provided by the NESDIS Joint Center for Satellite Data Assimilation (JCSDA). We thank Prasanjit Dash of NOAA/NESDIS STAR, Paul Van Delst and David Groff of JCSDA and Jerry Sullivan of NOAA/NESDIS STAR for the helpful discussion. The views, opinions, and findings contained in this report are those of the authors and should not be construed as an official NOAA or U.S. Government position, policy, or decision.

References

Cao, C., M. Weinreb, and J. Sullivan (2001). Solar contamination effects on the infrared channels of the advanced very high resolution radiometer. *J. Geophys. Res.*, 106, 33463–33469.

Dash, P. and A. Ignatov (2008). Validation of clear-sky radiances over oceans simulated with MODTRAN4.2 and global NCEP GDAS fields against NOAA15-18 and MetOp-A AVHRRs. Submitted to *Remote Sens. Environ*.

Donlon, C.J., P.J. Minnett, T.J. Gentlemann, I.J. Barton, B. Ward, and M.J. Murray (2002). Toward improved validation of satellite surface skin temperature measurements for climate research. *J. Clim.*, 15, 353–369.

Emery, W. J., D. J. Baldwin, P. Schlussel, and R. W. Reynolds (2001). Accuracy of in situ sea surface temperatures used to calibrate infrared satellite measurements. *J. Geophys. Res.*, 106, 2387–2405.

Flatau, P.J., R.L. Walko, and W.R. Cotton (1992). Polynomial fits to saturation vapor pressure. *J. Appl. Meteorol.*, 31, 1507–1513.

Goff, J.A. and S. Gratch (1946). Low-pressure properties of water from -160 to 212 °F. *Transactions of the American Society of Heating and Ventilating Engineers*, 95-122. Presented at the 52nd annual meeting of the ASHVE, New York.

Guildner, L., D.P. Johnson, and F.E. Jones (1976). Vapor pressure of water at its triple point. *J. Res. Natl. Bur. Stand.*, 80A, 505-521.

Ignatov, A., J. Sapper, I. Laszlo, N. Nalli, A. Harris, W. Pichel, A.E. Strong, E. Bayler, X. Li, and E. Maturi (2004). Global operational sea surface temperature and aerosol products from AVHRR: current status, diagnostics, and potential enhancements. *13th AMS Conference on Satellite Oceanography and Meteorology*, Norfolk, Virginia, 20–24 September 2004.

Masuda, K., T. Takashima, and Y. Takayama (1988). Emissivity of pure and sea waters for the model sea surface temperature in the infrared regions. *Remote Sens. Environ*., 24, 313–329.

May, D. A., M.M. Parmeter, D.S. Olszewski, and B.D. McKenzie (1998). Operational processing of satellite sea surface temperature retrievals at the Naval Oceanographic Office. *Bulletin of the American Meteorological Society*, 79, 397–407.

McClain, E. P., W.G. Pichel, and C.C. Walton (1985). Comparative performance of AVHRR-based multichannel sea surface temperatures. *J. Geophys. Res.*, 90, 11,587–11,601.

Merchant, C. J. and P. Le Borgne (2004). Retrieval of sea surface temperature from space, based on modeling of infrared radiative transfer: capabilities and limitations. *J. Atmos. Oceanic, Technol.*, 21, 1734–1746.

Moncet, J.-L., G. Uymin, and H.E. Snell (2004). Atmospheric radiance modeling using the Optimal. Spectral Sampling (OSS) method. *Proc. SPIE Int. Soc. Opt. Eng.*, 5425, 368–374.

Regulski, P.J. and D.L. Hartmann (2004). Simple experiments on the relationship of air temperature to SST in the Tropics. *15th Symposium on Global Change and Climate Variations*, AMS Annual Meeting, 14 January 2004.

Saunder, R., M. Matricardi, and P. Brunel (1999). An improved fast radiative transfer model for assimilation of satellite radiances observations. *Q. J. R. Meteorol. Soc.,* 125, 1407–1425.

Saunders, R., P. Rayer, P. Brunel, et al. (2007). A comparison of radiative transfer models for simulating Atmospheric Infrared Sounder (AIRS) radiance, *J. Geophys. Res.*, 112, D01S90, doi:10.1029/ 2006JD007088.

Sherlock, V. (1999). ISEM-6: Infrared surface emissivity model for RTTOV-6, EUMETSAT NWP SAF.

Wan, Z. and J. Dozier (1996). A generalized split-window algorithm for retrieving land-surface

temperature from space. *IEEE Trans. Geosci. Remote Sens.,* 34, 892–905.

Walton, C.C., W.G. Pichel, J.F. Sapper, and D.A. May (1998). The development and operational applications of nonlinear algorithms for the measurement of sea surface temperatures with the NOAA polar-orbiting environmental satellites. *J. Geophys. Res., 103,* 27, 999–28,012.

Watts, P.D., M.R. Allen, and T.J. Nightingale (1996). Wind speed effects on sea surface emission and reflection for the Along Track Scanning Radiometer. *J. Atmos. Oceanic, Technol.*, 13, 126–141.

Weng, F. (2005). Development of JCSDA Community Radiative Transfer Model (CRTM). *The 14th International TOVS Study Conference*, Beijing, China, May 25–31, 2005.

Wu, X. and W.L. Smith (1997). Emissivity of rough sea surface for 8–13 um: modeling and verification. *Appl. Opt.*, 36, 2609–2618.

Table 1: Comparison of SVP value between Goff-Gratch (1946) approach and polynomial fit of data from Flatau et al. (1976)

T (K)	Flatau et al (1976) (hPa)	Goff-Gratch(1946) (hPa)	(F-G)/F (%)
188	5.21E-04	4.49E-04	13.7929
198	2.48E-03	2.30E-03	7.6028
208	1.00E-02	9.64E-03	3.9012
218	3.53E-02	3.46E-02	2.0725
228	0.1105	0.1092	1.1922
238	0.3108	0.3089	0.593
248	0.7975	0.7954	0.2603
258	1.8898	1.8867	0.1647
268	4.1718	4.1640	0.1859
278	8.6408	8.6224	0.2134
288	16.9019	16.8690	0.1948
298	31.4110	31.3700	0.1305
308	55.7698	55.7408	0.0519
318	95.0715	95.0689	0.0027

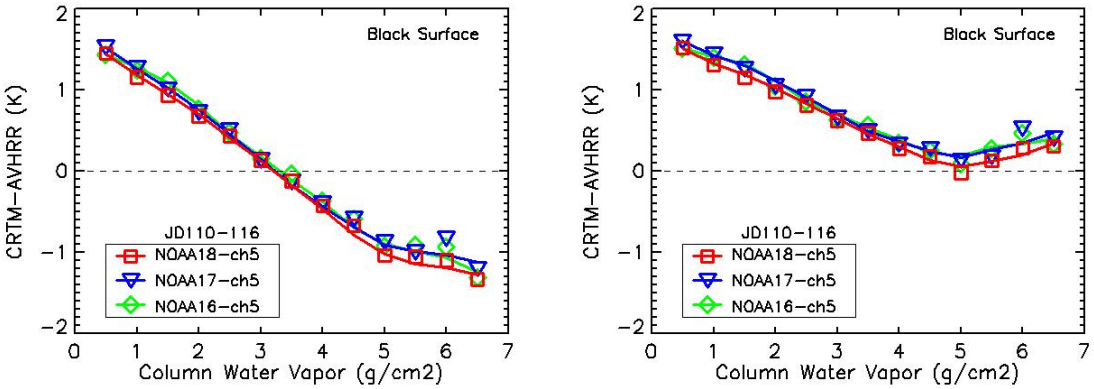

Figure 1. The mean M-O biases in AVHRR Ch5 onboard three NOAA platforms as a function of column water vapor: initial implementation (left) and corrected implementation (right). The surface is black in both cases. One week of global data from 19–25 April 2006 is used (see discussion in section 3.1 for detail).

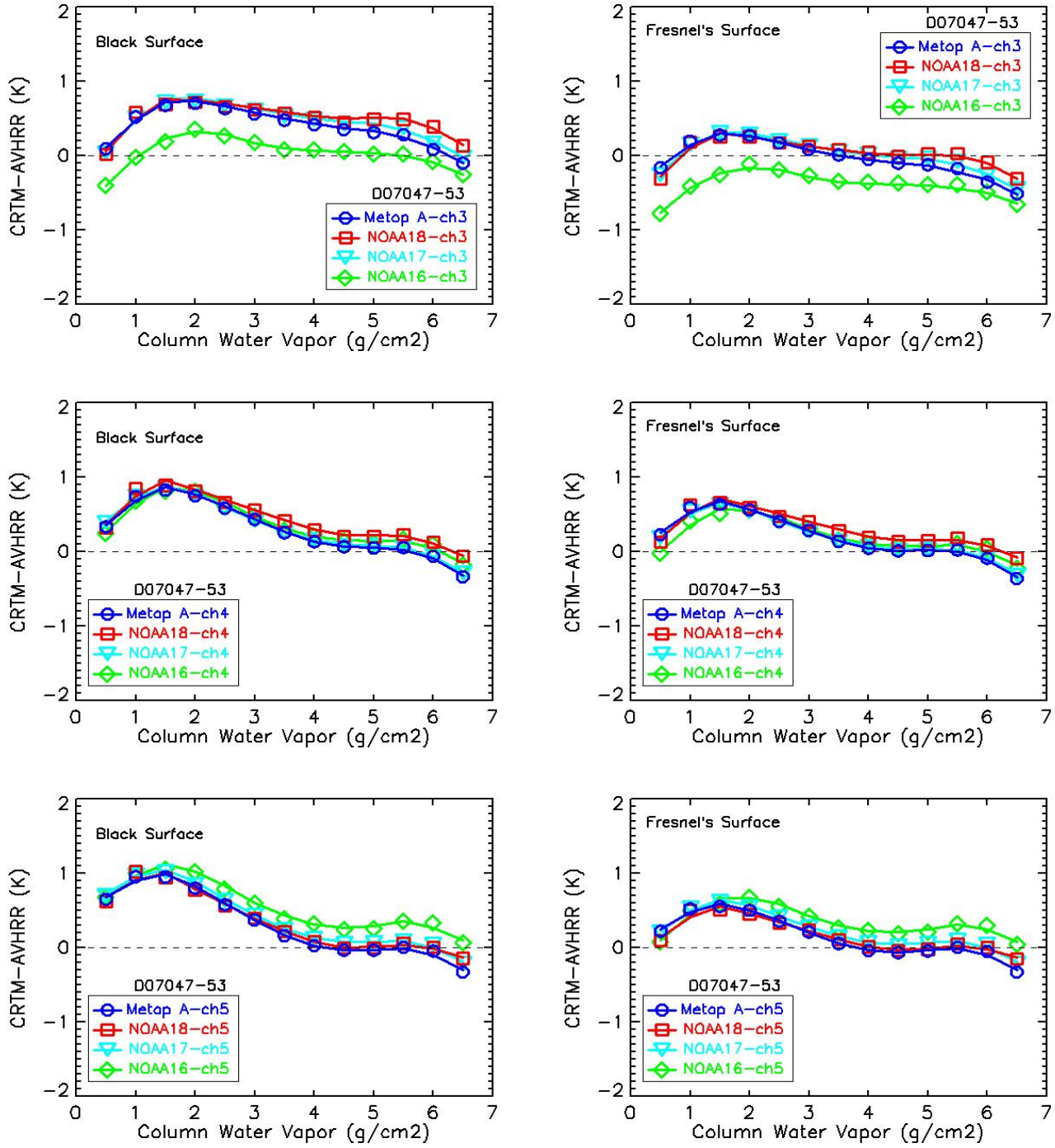

Figure 2. The same as in Figure 1 but for three AVHRR bands onboard four platforms: black surface (left) and Fresnel's surface (right). One week of global data from 16–22 February 2007 is used. The amplitude of the water vapor dependence is smaller for Fresnel's model.

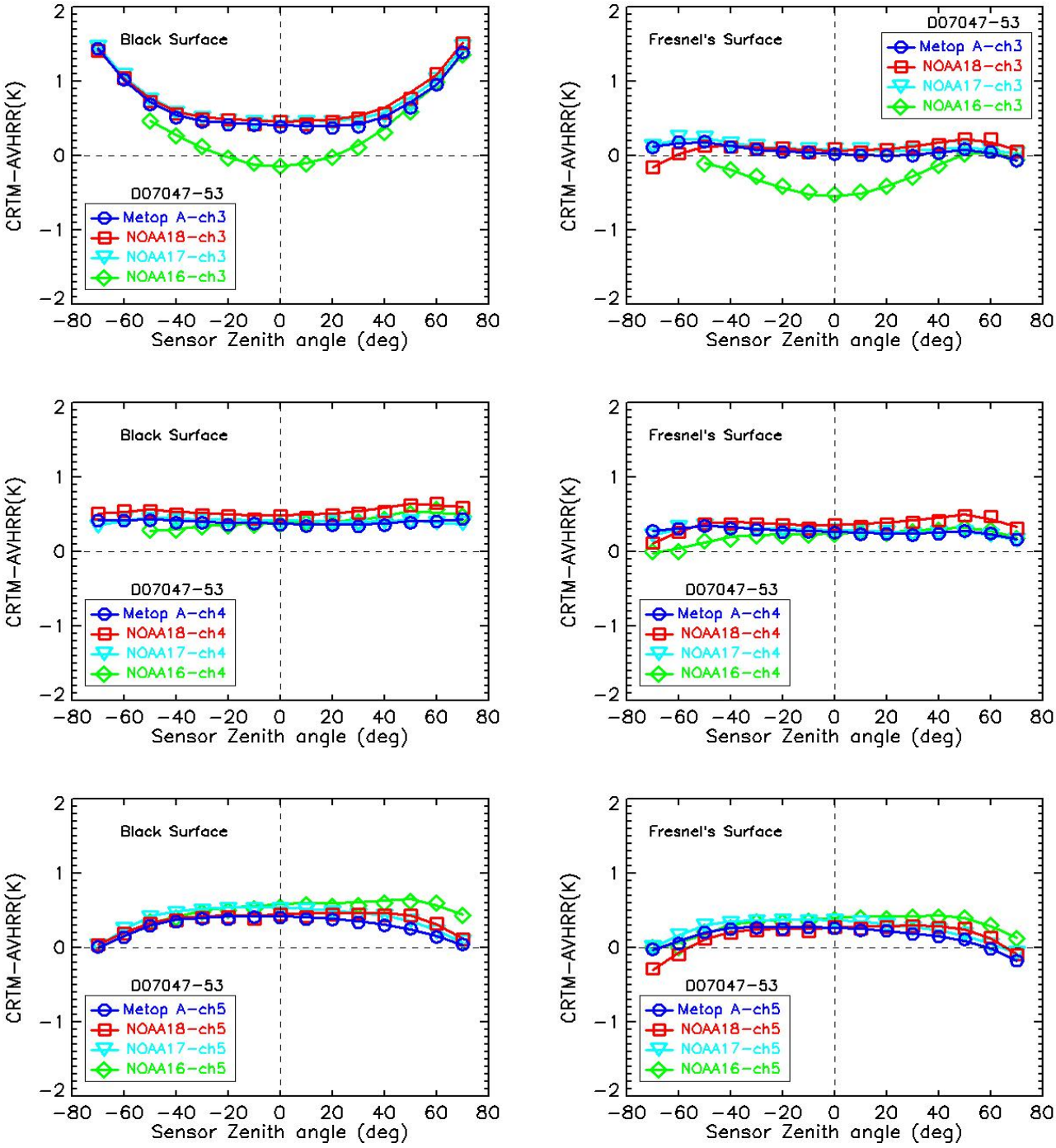

Figure 3. The same as in Figure 2 but as a function of view zenith angle. The M-O bias and its amplitude are consistently smaller when Fresnel's surface model is used.

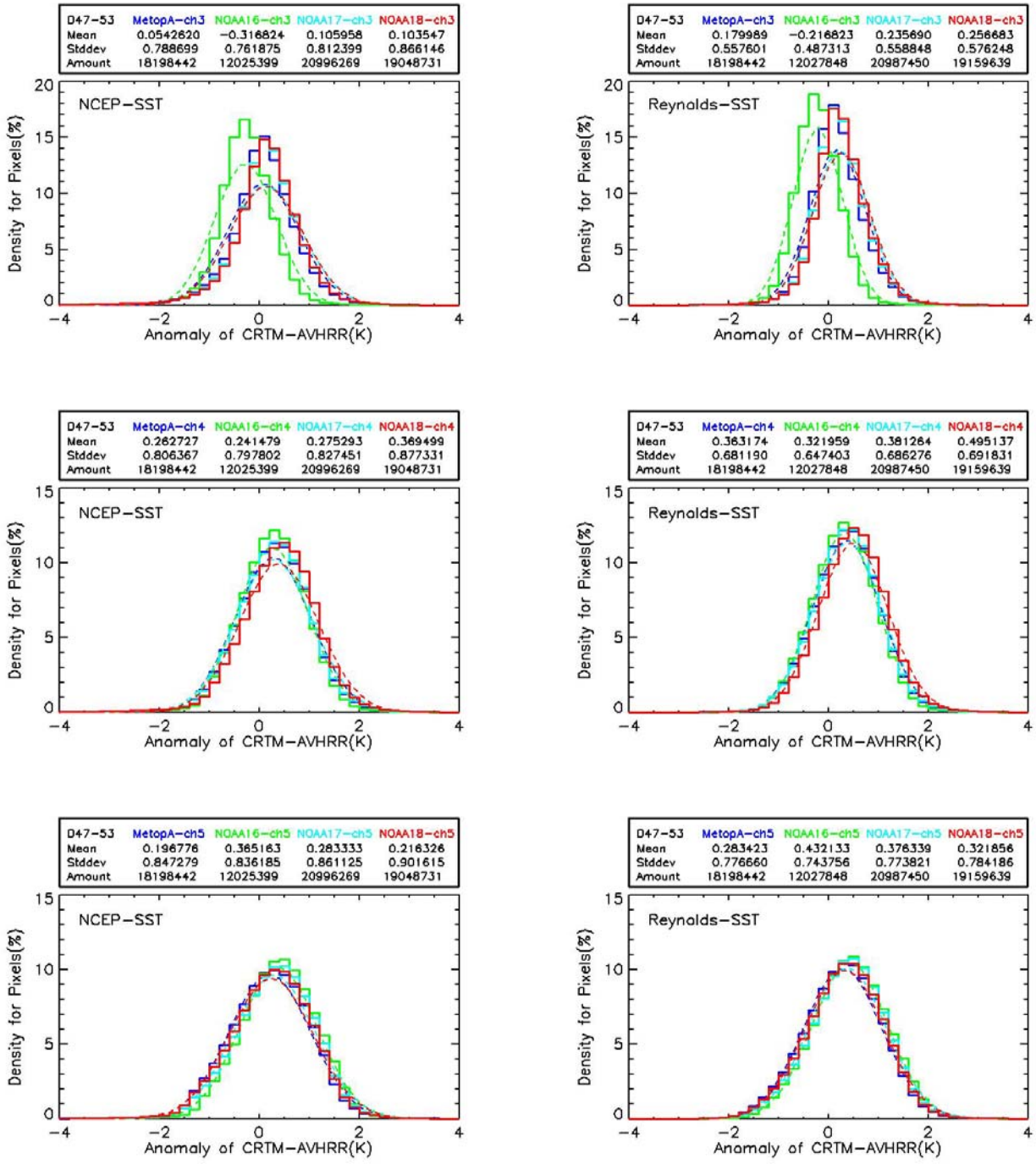

Figure 4. Global histograms of the M-O bias for the week of 16–22 February 2007: NCEP-SST (left) and Reynolds-SST (right). For Reynolds SST, the histograms are consistently narrower than for NCEP SST. Respective mean biases are 0.18–0.26 versus 0.05–0.11 K in Ch3B; 0.32–0.50 versus 0.24–0.37 K in Ch4; and 0.28–0.33 K versus 0.20–0.37 K. Respective standard deviations are 0.49–0.58 versus 0.76–0.87 K in Ch3B; 0.65–0.69 versus 0.80–0.88 K in Ch4; and 0.74–0.78 versus 0.84–0.90 k in Ch5.

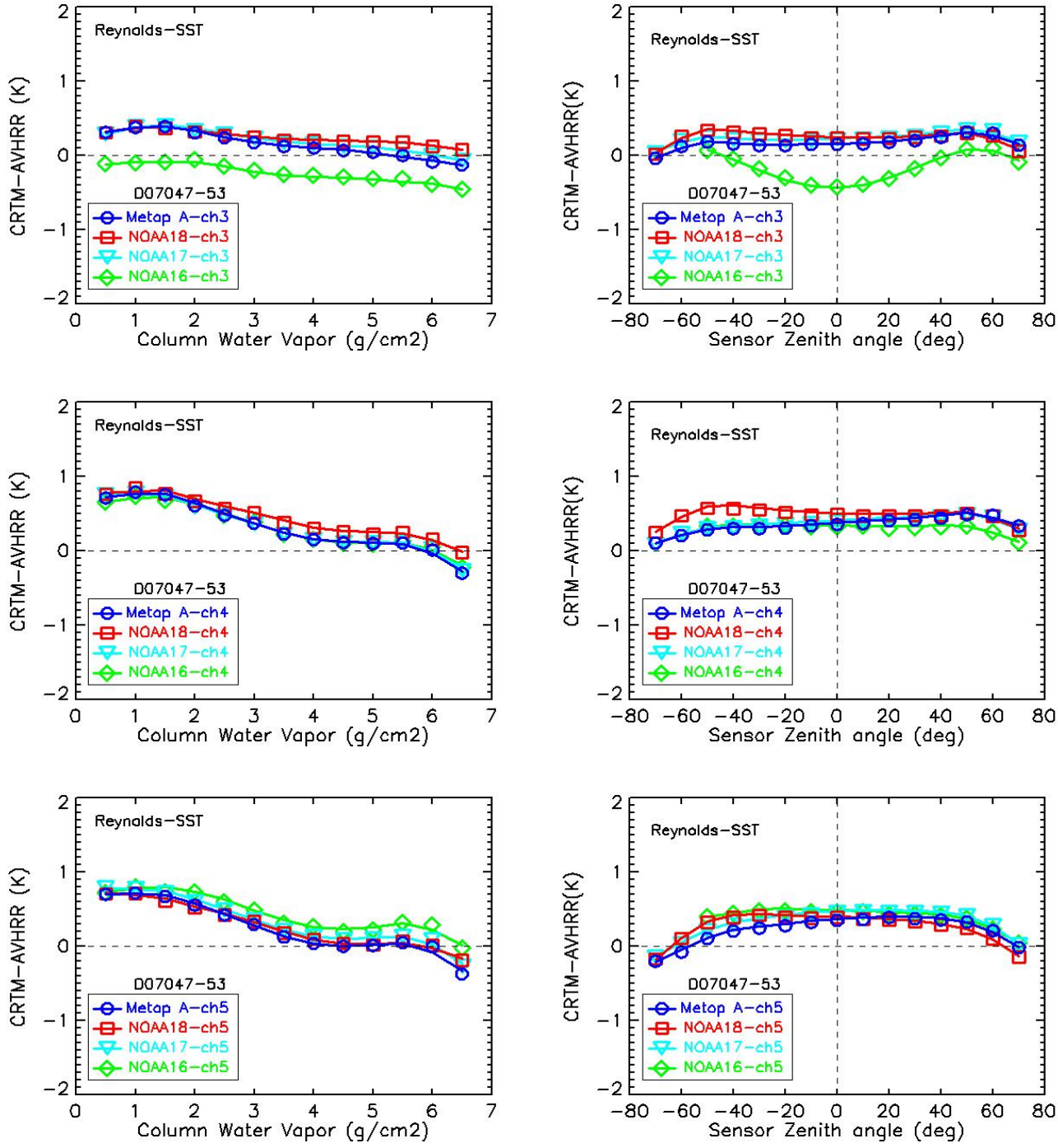

Figure 5. Left: the same as in Figure 2 (right). Right: the same as in Figure 3 (right) but for Reynolds SST. Water vapor and view zenith angle dependencies improve if Reynolds SST is used instead of NCEP SST.

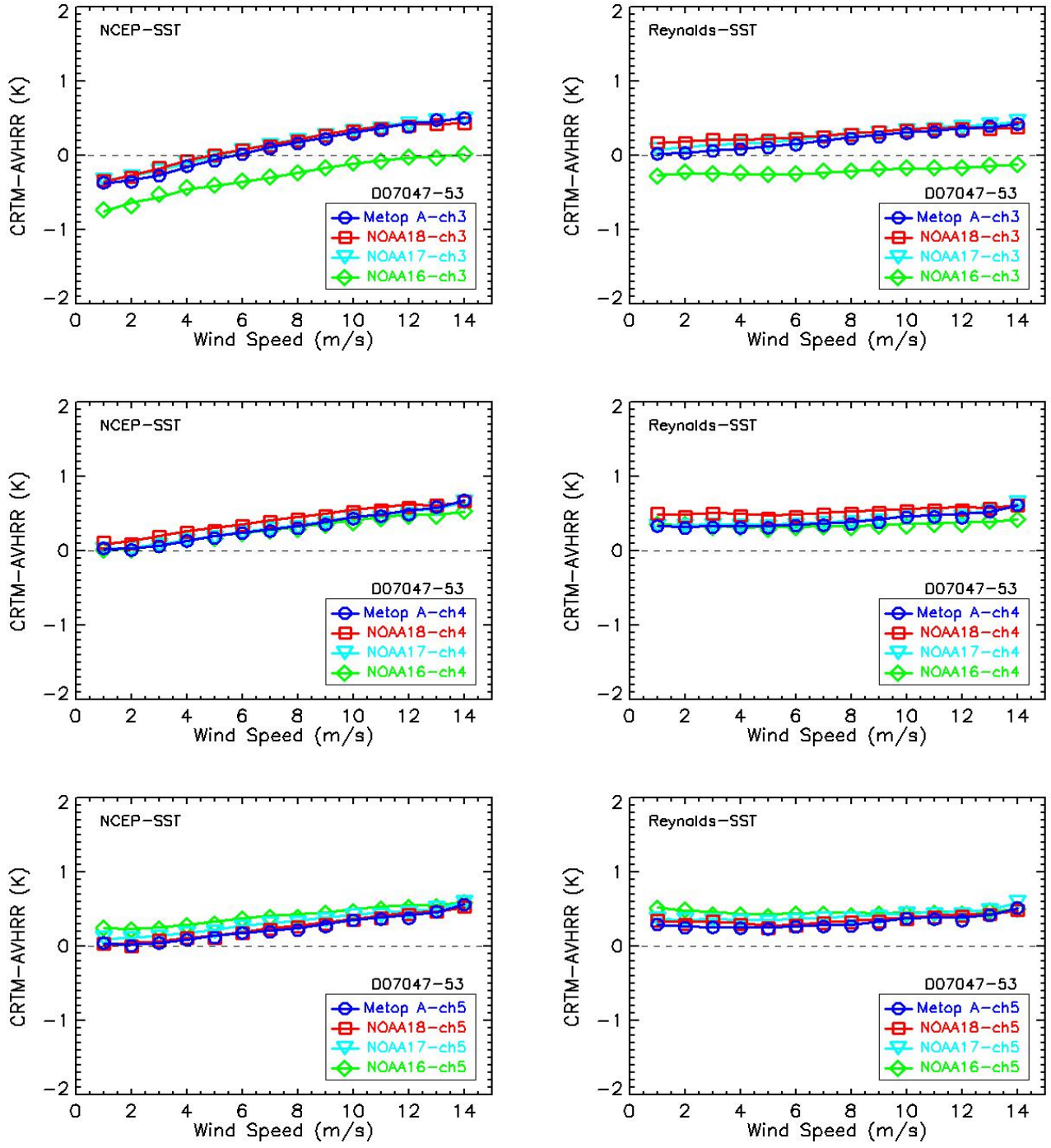

Figure 6. The same as in Figure 5 but as a function of wind speed. Left: NCEP SST; right: Reynolds SST. The amplitude of the wind speed dependence is significantly reduced in case of Reynolds SST. (See discussion in section 3.3.)

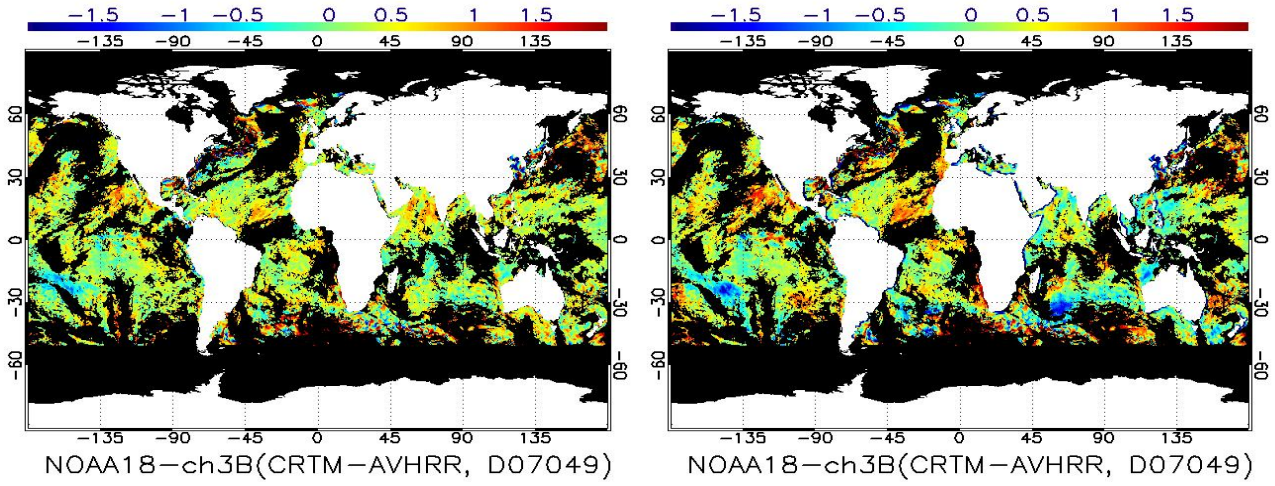

Figure 7. Global distribution of M-O biases for NOAA18-Ch3B for one day of 18 February 2007. Left: Reynolds-SST; right: NCEP-SST used as input to CRTM.

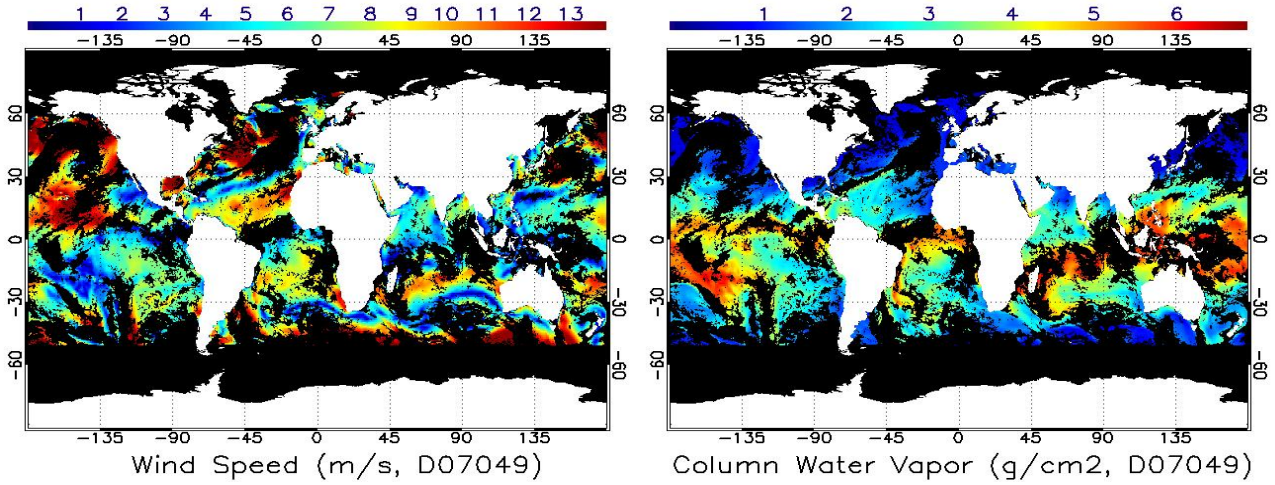

Figure 8. Global distribution of wind speed corresponding to Figure 7.

Figure 9. Global distribution of column water vapor corresponding to Figure 7.

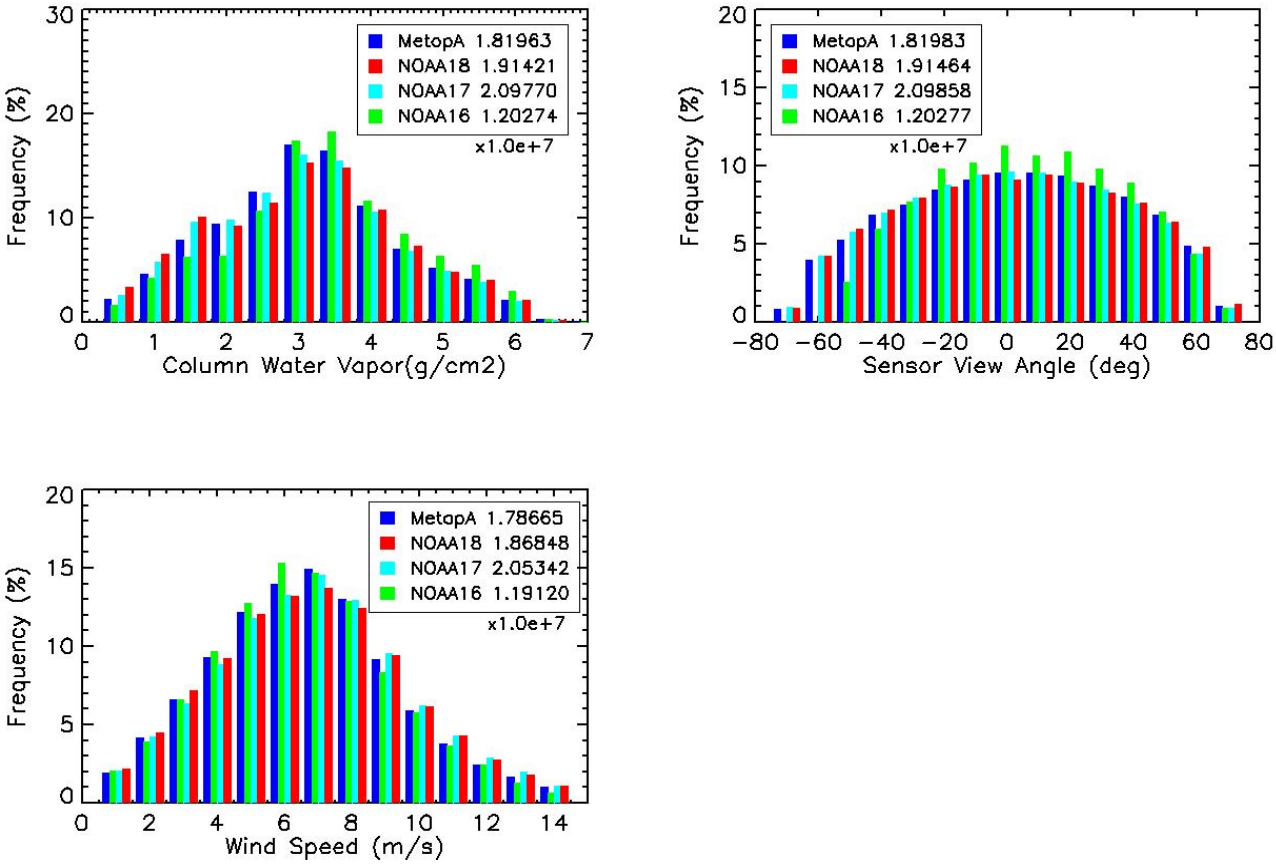

Figure 10. Histograms of column water vapor (upper left, bin size=0.5g/cm^2), sensor zenith angle (upper right, bin size=10º) and wind speed (down left, bin size=1m/s) corresponding to Figures 5 and 6 (right), respectively.

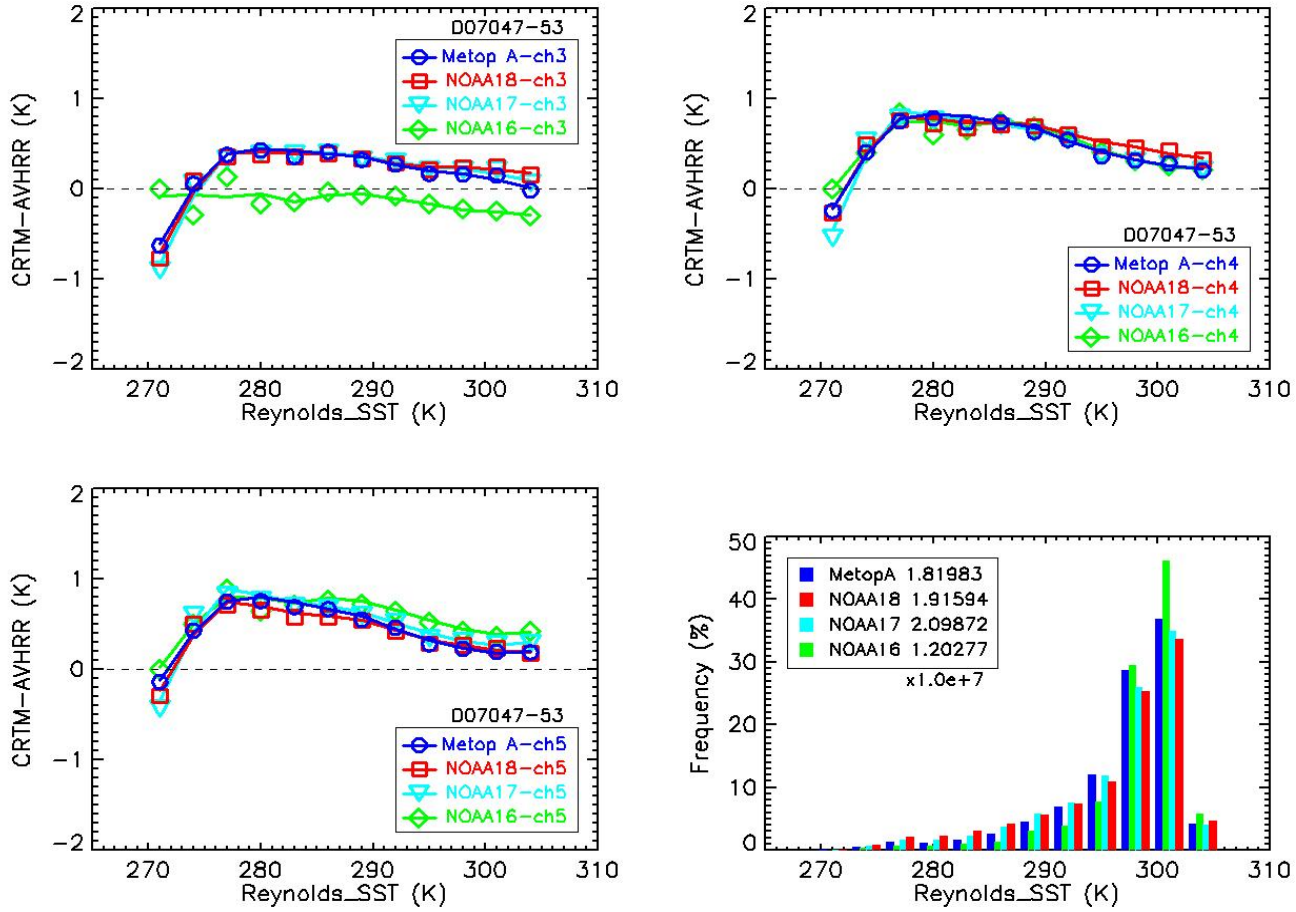

Figure 11. SST dependence of the M-O bias and SST histogram with bin size 3K.

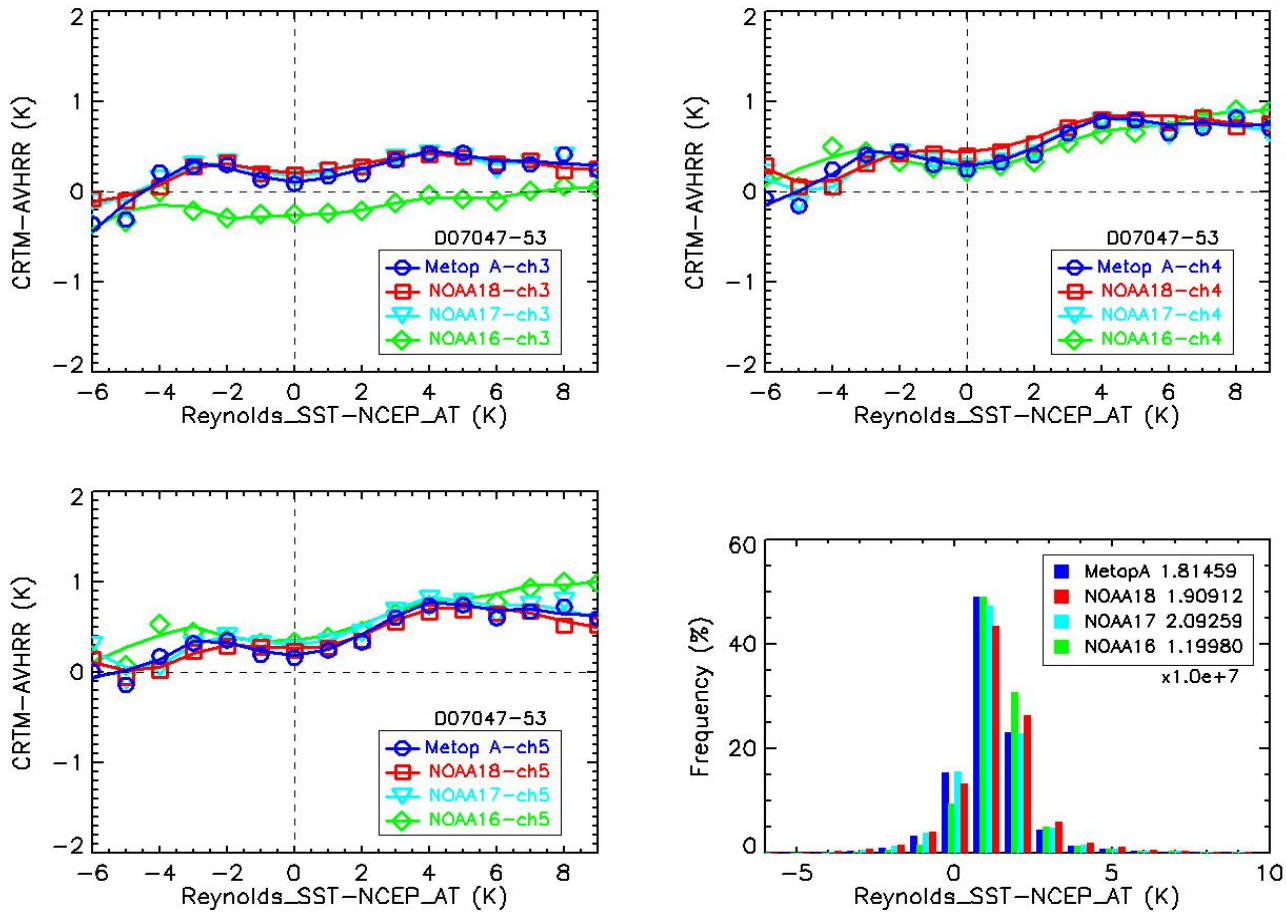

Figure 12. Sea-air temperature difference dependence of M-O bias and corresponding SST-AT histogram (bin size 1K). (AT = near-surface air temperature)

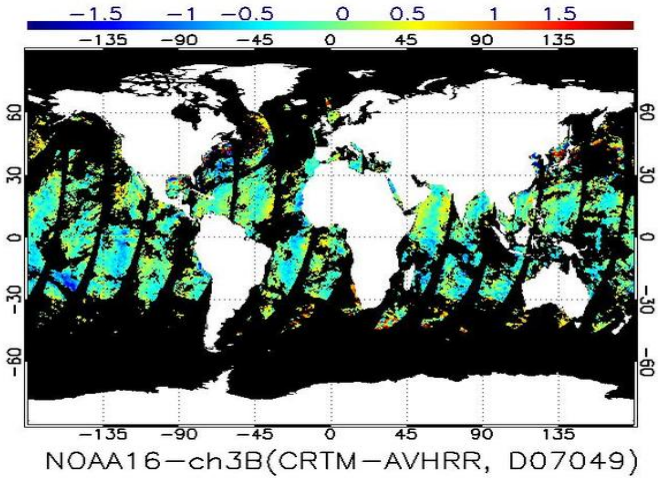

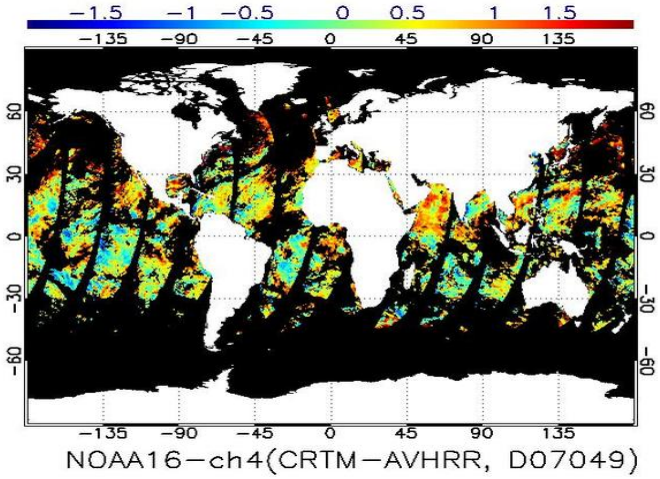

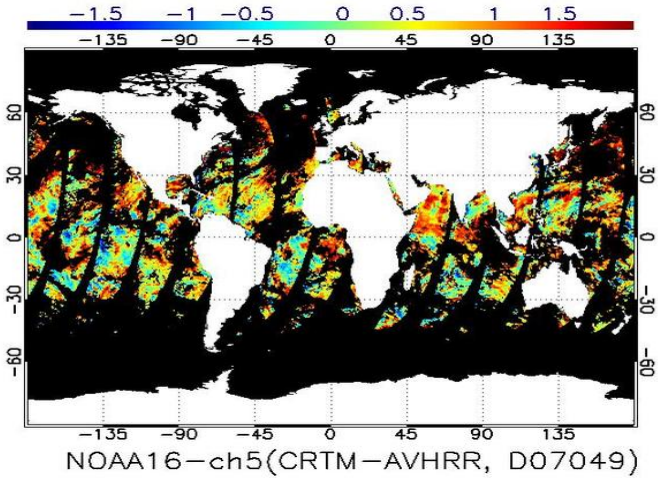

Figure 13. Global maps of M-O biases for NOAA-16 in three AVHRR bands in 18 February 2007.

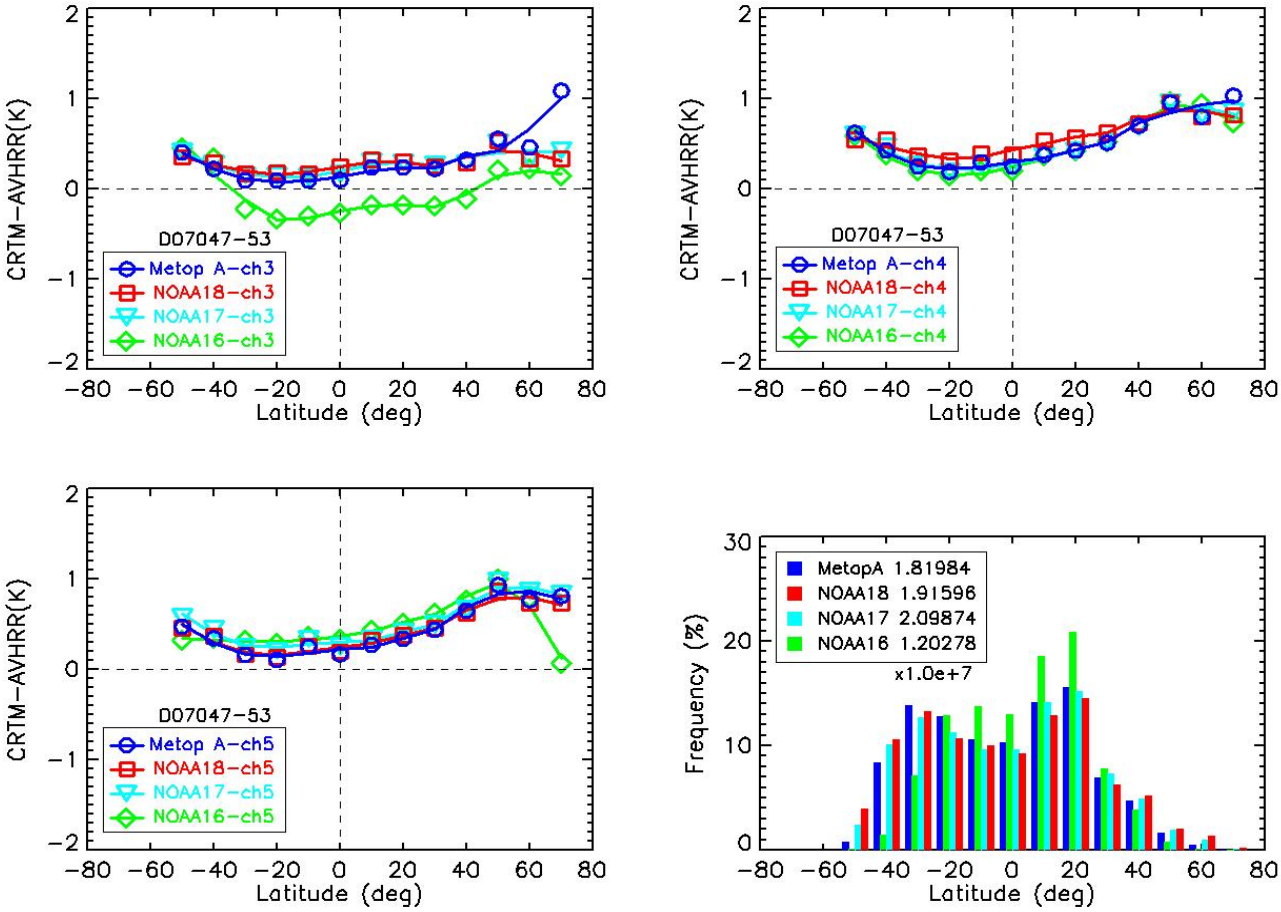

Figure 14. Zonal dependence of M-O bias and its histogram (bin size: 10º) for one week of 16-22 February 2007.

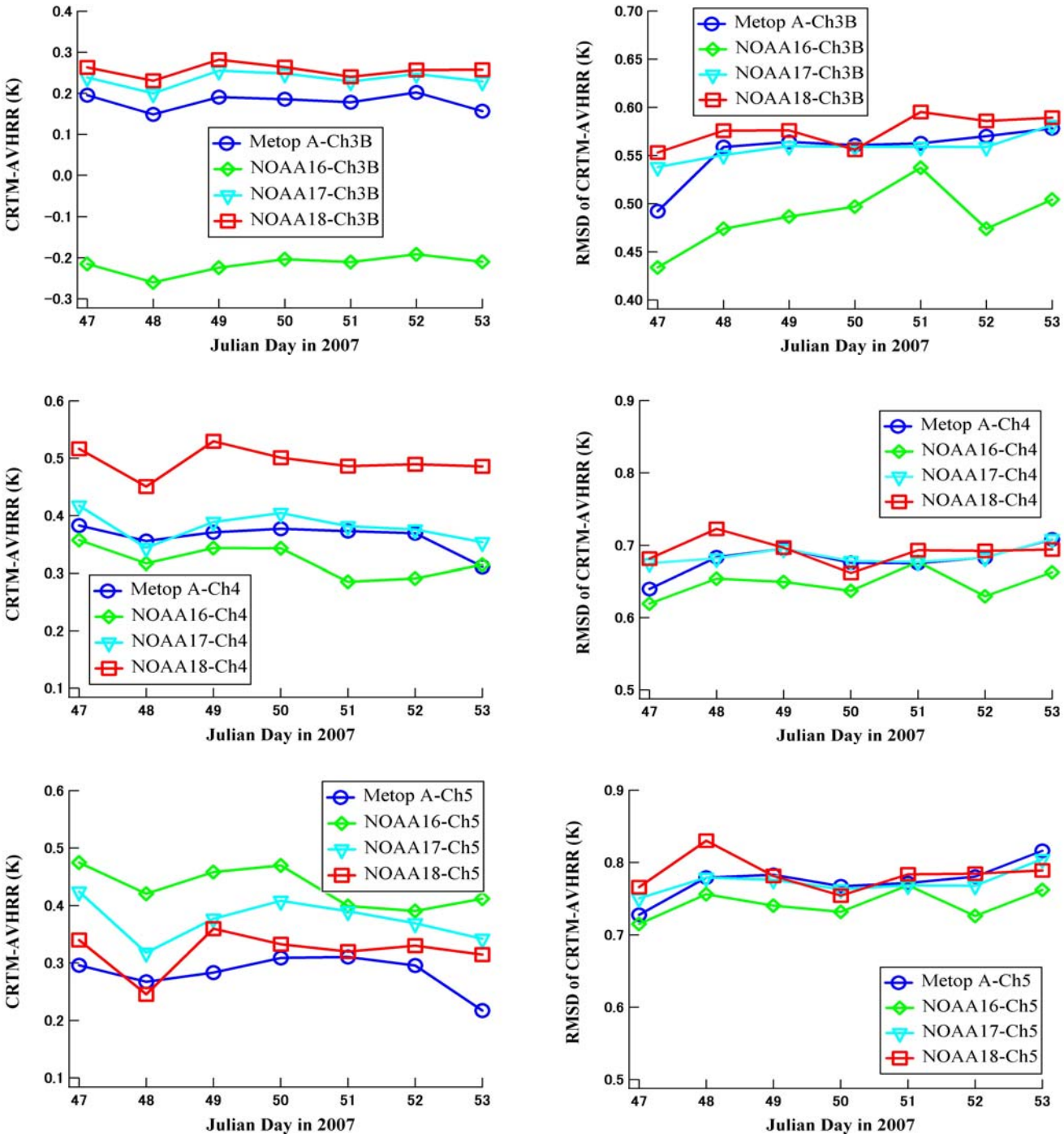

Figure 15. Time series of the (left) mean M-O bias and (right) RMSD for one week of global observations from 16–22 February 2007.